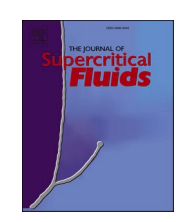
ELSEVIER

Contents lists available at ScienceDirect

# The Journal of Supercritical Fluids

journal homepage: www.elsevier.com/locate/supflu





# Multilayer microcellular structures by steam-assisted one-step supercritical CO<sub>2</sub> foaming of PMMA

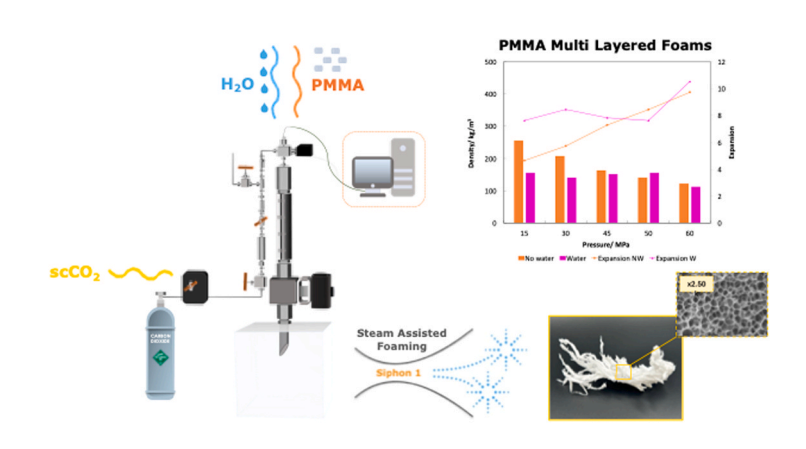
Aránzazu Redondo <sup>a</sup> , Judith Martín-de León <sup>a,b</sup>, Michel Simard <sup>c</sup>, Danilo Cantero <sup>a,\*</sup>

- a The Institute of Bioeconomy, Department of Chemical Engineering and Environmental Technology, University of Valladolid, Valladolid 47011, Spain
- <sup>b</sup> Cellular Materials Laboratory (CellMat), Condensed Matter Physics Department, University of Valladolid, Valladolid 47011, Spain
- <sup>c</sup> Department of Mechanical Engineering, Villanova University, Villanova, PA 19085, USA

#### HIGHLIGHTS

- One-step steam-assisted scCO<sub>2</sub> foaming enables the production of multilayer PMMA foams.
- Foam morphology and porosity are controlled by pressure, temperature, and time.
- Subcritical water reduces structural defects through in situ plasticization.
- Steam-assisted foaming boosts pressuredrop rates promoting foaming at lower pressure.

#### GRAPHICAL ABSTRACT



# ARTICLE INFO

Keywords: Plastics Polymers Foaming Carbon Dioxide Explosion Energy Efficiency

## ABSTRACT

In this work, we introduce a one-step steam-assisted supercritical  $CO_2$  foaming process to create multilayer PMMA foams with tunable pore structures. The method operates entirely above the polymer's effective glass transition temperature (125 °C), allowing saturation and foaming to take place simultaneously in a matter of minutes. By adding subcritical water before saturation, the system triggers a steam explosion during depressurization, leading to much faster pressure drops (up to 40 % faster), improved nucleation, and a notable reduction in structural defects. As a result, foams with more uniform cells, finer pore sizes (2.3  $\mu$ m), and lower densities (91 kg / m³; +10 X expansion) are obtained even at moderate pressures. A particularly interesting outcome is the formation of multilayer architectures: polymer pellets with different levels of  $CO_2$  uptake fuse naturally into foams with distinct porosities across layers. This opens new opportunities for designing multifunctional materials, where different layers could be tailored for specific mechanical, thermal, or acoustic roles. The creation of multilayer is mostly attributed by the combination of one-step foaming above the Tg of the polymer together with a pellet sudden ejection from the autoclave while foaming and freezing the structure. Overall, the steam-assisted approach offers a scalable and energy-efficient pathway to produce polymer foams with customized microstructures and properties.

E-mail address: danilo.cantero@uva.es (D. Cantero).

#### https://doi.org/10.1016/j.supflu.2025.106746

 $<sup>^{\</sup>star}$  Corresponding author.

#### 1. Introduction

The microcellular foams are thermoplastic polymers that contain cells typically on the order of 1-10 µm in size, with cell densities exceeding 10<sup>9</sup> cells / cm<sup>3</sup>. By introducing a high-volume fraction of finely distributed voids within the polymer matrix, these materials exhibit significantly reduced density compared to their solid counterparts while preserving desirable mechanical attributes [1–4]. Various amorphous polymers—such as polyvinyl chloride (PVC) [5], polycarbonate (PC) [6,7], acrylonitrile-butadiene-styrene (ABS) [8,9], polyethylene terephthalate (PET) [10-12], polylactic acid (PLA) [13], polystyrene (PS) [14-16] and polymethylmethacrylate (PMMA) [17–19] —have been employed to produce microcellular foams. Owing to their balance of high stiffness-to-weight ratio, impact resistance, thermal stability, and improved fatigue life, these foams are applied in acoustic insulation, lightweight structural components for automotive and aerospace, energy-absorbing sports equipment, and microelectronic devices [20,21].

Although microcellular foams can be produced through various routes, gas dissolution foaming has gathered significant attention for its environmental advantages [22,23]. In this process, the polymer is saturated with an inert blowing agent, most commonly CO2 in a supercritical state (scCO<sub>2</sub>) [22,24] due to its non-toxic, non-flammable nature and relatively low critical temperature and pressure. Upon rapid depressurization, the polymer-gas solution separates into distinct phases as CO2 transitions from supercritical fluid to gas. Simultaneously, heating the material above its effective glass transition temperature (Tg, eff) ensures adequate melt strength and viscosity control, facilitating stable cell nucleation and growth with small pores [1]. Traditionally, microcellular gas foaming is executed in two discrete steps: (i) saturation below Tg,eff, followed by (ii) a post-foaming expansion (bubble formation and growth) phase above Tg,eff [5,25-28]. This approach, though robust, demands long cycle times and precise thermal management to avoid pore collapse or poor cell distribution. A different approach is the process conducted in one-step, in which the saturation is carried out above the T<sub>g,eff</sub> of the polymer, and the foaming takes place during the depressurization of the system [17,29-33].

Despite these advances, achieving consistent pore structure and controlling the nucleation process remain challenging, particularly at industrial scales. Moreover, concerns regarding energy consumption and process efficiency drive the search for new methods that further reduce the environmental footprint of polymer foaming. Purely CO<sub>2</sub>-driven processes can face additional obstacles such as uneven heat transfer, restricted cell-growth kinetics, and potential cell collapse if depressurization and temperature are not finely tuned [34,35].

In response to these limitations, we developed a one-step, steam-assisted scCO<sub>2</sub> foaming method. The process operates entirely above the Tg,eff of PMMA (at 125  $^{\circ}\text{C}$ ), allowing saturation and foaming to occur simultaneously within minutes—significantly reducing cycle time. The

novelty lies in introducing subcritical water into the high-pressure vessel. Subcritical water has a lower dielectric constant than liquid water at ambient conditions, allowing partial miscibility with non-polar fluids like CO2 at near-critical conditions [36-38]. Under these elevated temperatures, water also exhibits higher ionic product and diffusivity [39], potentially enhancing fluid-polymer interactions [33–35]. Upon depressurization, this water explosively vaporizes, generating steam that increases the pressure drop rates (PDRs) in around one order of magnitude (~30 ×), enhances nucleation, and improves foam uniformity. This process delivers a more intense Joule-Thomson cooling and expansion effect than CO2 alone. This "steam explosion" also generates additional shear energy, which can promote more extensive foaming, reduce pore collapse, and improve cell-size uniformity. The presence of water can also lower the glass transition temperature of the polymer further, facilitating expansion at milder processing conditions. Such conditions—high CO2 pressures up to 60 MPa in the presence of hot compressed water—have not been previously reported in the literature.

PMMA is particularly suitable for this process due to its high CO<sub>2</sub>-philicity [3,19] and stability under hydrothermal conditions up to 200 °C [40]. While water has occasionally been used as a dispersant to prevent agglomeration during foaming [6], its role here is radically redefined—as an active agent in driving nucleation and expansion. Subcritical water not only facilitates more intense Joule—Thomson cooling during depressurization but also acts as a plasticizer, lowering Tg locally and improving foam expansion dynamics.

Importantly, the process yields an unexpected material architecture: multilayer foams formed by partial saturation of pellets with different sizes. As these pellets fuse during explosive expansion, they form macroscopically coherent foams with spatially varying porosity. This gradient morphology is achieved in situ, without lamination or additional processing steps. Each layer exhibits uniform internal porosity, while the overall material presents a controlled pore-size stratification. These multilayer foams represent a new class of high-performance cellular materials with potential applications in lightweight sandwich structures, thermal barriers, acoustic dampening, and beyond.

This study offers a systematic analysis of the key parameters influencing this new process: saturation pressure, time, and the presence of water. Through detailed scanning electron microscopy (SEM), differential scanning calorimetry (DSC), and density analyses, we show how this strategy leads to foams with lower density ( $\sim 100~{\rm kg}~/{\rm m}^3$ ), smaller pore sizes ( $<3~\mu m$ ), and higher cell nucleation densities compared to traditional methods. Moreover, we highlight how water addition significantly boosts PDR and enables uniform foaming even at reduced pressures. This work advances a transformative approach to polymer foaming by combining steam-assisted depressurization with one-step saturation above Tg. It demonstrates not only improvements in processing efficiency and material performance but also unveils a new class of multilayer foam architectures that could reshape the design of cellular polymer systems in engineering applications.

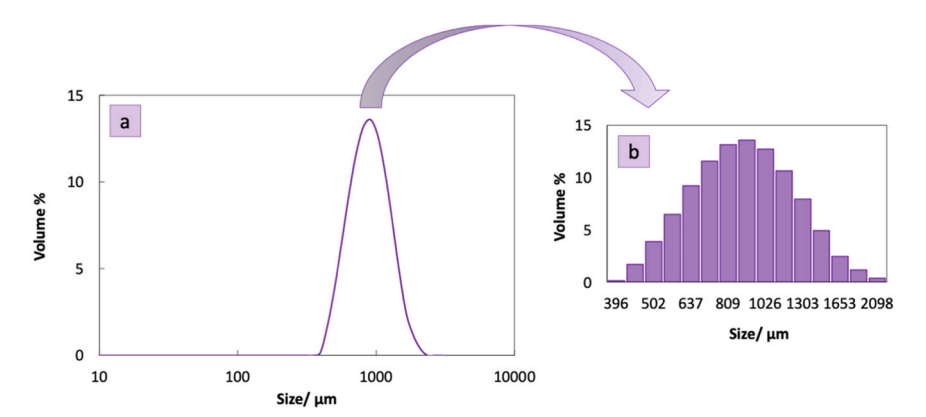


Fig. 1. Pellet distribution of milled PMMA: a) Graph on a logarithmic scale representing an unimodal distribution; b) Bar graph illustrating the sizes of the pellets.

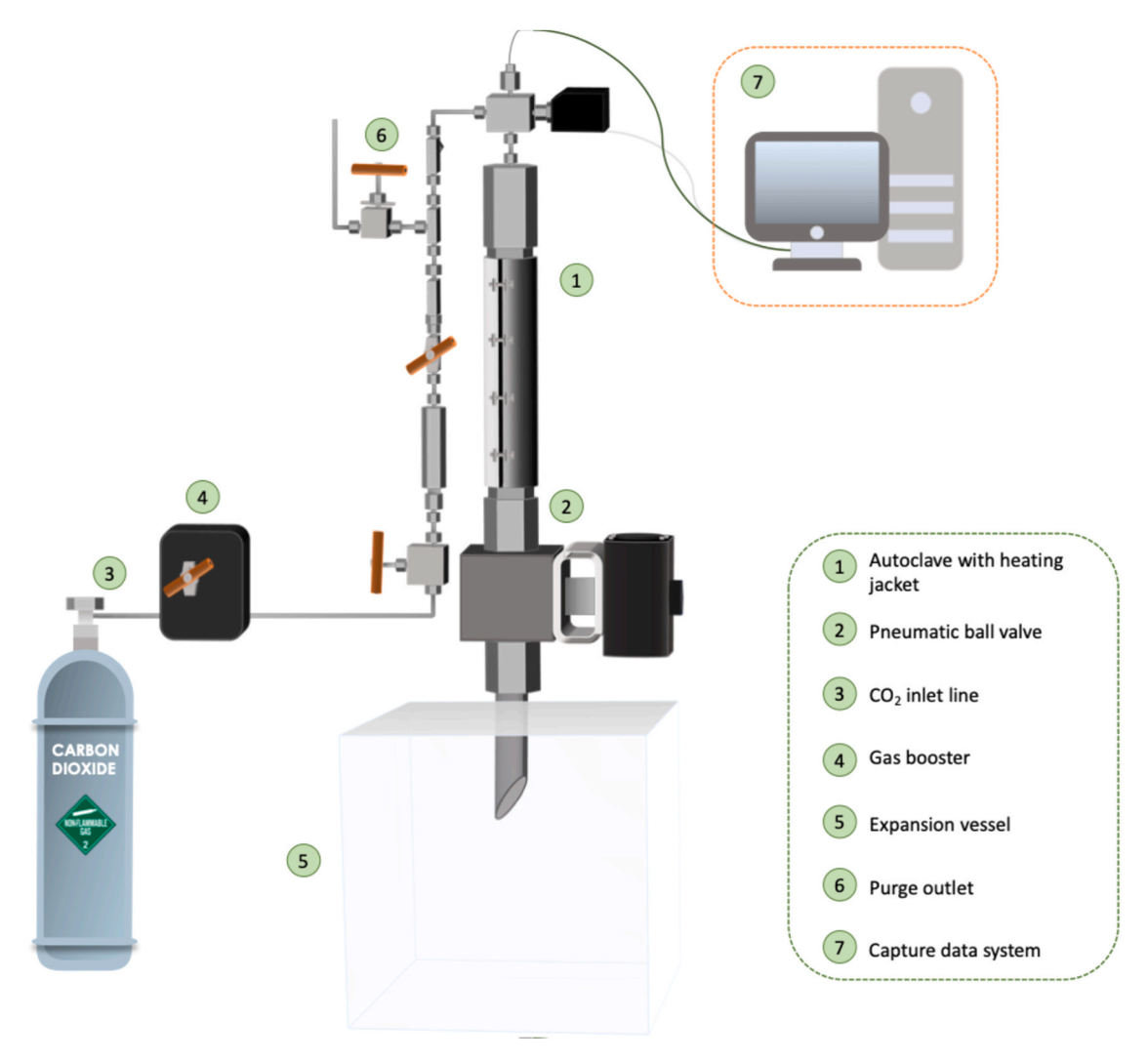


Fig. 2. Rendering of Siphon 1 system set up.

### 2. Experimental

#### 2.1. Material and reagents

PMMA Plexiglas® grade 7 N of Roehm GmbH was supplied by PLEXIGLAS® Evonik Industries (Essen, Germany) as pellets (2.35 mm diameter x 3 mm long). This polymer has a  $T_g$  of 110 °C and a density ( $\rho$ ) of 1190 kg /  $m^3$  (as measured at 23 °C and 50 % relative humidity). As the blowing foaming agent, high purity CO $_2$  (>99.9 %) was used from Linde Gas Spain. Ultrapure water from a Milli-Q® water purification system was used (18.2 MW·cm).

## 2.2. Sample preparation

PMMA was size reduced into smaller pellets with a cutting mill SM100 from Retsch GmbH® (Haan, Germany). The material was sieved through a 2 mm sieve. Consequently, pellets were  $<\!2\,\mathrm{mm}$  in diameter (irregular shapes from the mill), and they were used directly for the foaming experiments.

The feedstock used in the foaming experiments was analyzed to understand how particle size might affect gas diffusion and foam formation. Fig. 1 presents the particle size distribution (PSD) of the ground PMMA pellets on a logarithmic scale. The distribution appears unimodal, centered around  $1000\,\mu m$  (Fig. 1a). A more detailed examination reveals that particle diameters range from approximately  $300\,\mu m$  to

 $2000\,\mu m$  (Fig. 1b), indicating a reasonably homogeneous milling process despite having a relatively broad overall size window.

This PSD has direct implications for the foaming process: smaller particles can saturate with  $CO_2$  more quickly, while larger ones may remain partially saturated under the same conditions. Consequently, any morphological differences observed in the final foamed products could stem, in part, from this inherent particle-to-particle variation. The subsequent sections evaluate how factors such as pressure, time, presence of water, and pellet size interplay to yield distinctive foam structures.

## 2.3. Samples production

#### 2.3.1. Equipment

A custom-designed batch system (hereafter called "Siphon 1") was developed by PressTech in collaboration with the University of Villanova for the saturation and foaming of polymers using  $CO_2$  and hot compressed water. A schematic diagram of this setup is provided in Fig. 2.

At the core of Siphon 1 is a 65 mL autoclave (High Pressure Equipment Co., maximum working conditions: 69 MPa at 200  $^{\circ}$ C) used as the primary pressure vessel (#1). The autoclave is surrounded by an electrically heated jacket (Ihne & Tesch), with temperature regulation handled by a Hillesheim HT-62–20P control system. This allows precise control of the saturation/foaming temperature at up to 200  $^{\circ}$ C.

**Table 1**Foaming experimental conditions for pressure test. NW: no water; W: water; X: purging NW experiment.

Test	P <sub>sat</sub> [MPa]	$H_2O$	$T_{sat}$ [°C]	t <sub>sat</sub> [min]
1	15	NW	125	60
2	30	NW	125	60
3	45	NW	125	60
4	50	NW	125	60
5	60	NW	125	60
6	15	W	125	60
7	30	W	125	60
8	45	W	125	60
9	50	W	125	60
10	60	W	125	60
X	45	NW	125	60

High-pressure CO<sub>2</sub> (#3) is supplied to the autoclave by a pneumatically driven gas booster (#4) (Maximator, model DLE 75–1-UU-C). The system pressure is initially ramped up to the desired saturation pressure. A pneumatic full-port ball valve (High Pressure Equipment Co.) is installed at the bottom of the autoclave to hold and then rapidly release the pressure (#2). Once opened, this valve allows a near-instant depressurization, forcibly ejecting the foamed polymer into a large expansion vessel (dimensions:  $60~\text{cm} \times 50~\text{cm} \times 70~\text{cm}$ ) where the expanded CO<sub>2</sub> is safely vented (#5). If a more gradual depressurization is ever required (e.g., to prevent excessive foaming or for specific experimental conditions), a separate purge valve is included downstream to bleed off pressure more slowly (#6).

To monitor process conditions in real time, a pressure sensor (WIKA) is mounted on top of the autoclave. Two thermocouples (Thermoexpert) measure temperature at critical points in the system:

- 1. Top of the autoclave (saturation/foaming temperature),
- 2. Inside the expansion vessel (downstream of the ball valve), capturing the temperature during rapid polymer ejection and cooling.

All pressure and temperature signals are captured and recorded by a PicoLog data logger (Pico Technology), enabling precise tracking of the experimental profile (#7). Through these measurements, the pressure drop rate (PDR) and temperature transients can be correlated with the resulting foam morphology.

This integrated setup ensures a reproducible and robust experimental platform for one-step saturation and foaming at high pressures and elevated temperatures, accommodating subcritical water in addition to supercritical  $\mathrm{CO}_z$ , and enabling safe handling of the gas and any steam generated during depressurization.

## 2.3.2. Foaming tests

A one-step saturation and foaming process was used throughout this work, maintaining the polymer above its effective glass transition temperature so that foaming occurred upon rapid depressurization. Two main sets of experiments were conducted to study (1) the effect of saturation pressure, and (2) the effect of saturation time. A fixed water: polymer mass ratio of 1:1 (10 g each) was used in all steam-assisted runs. This loading was chosen to reliably generate a strong steam impulse during rapid depressurization, provide sufficient thermal quenching capacity to arrest cell growth, and allow direct comparison with nowater controls while varying pressure and saturation time. The effect of water loading itself is the subject of ongoing work and was held constant here to preserve experimental clarity.

2.3.2.1. Pressure variation experiments. Table 1 summarizes the conditions used to examine pressure effects on PMMA foaming at 125 °C. The polymer was foamed with and without added water—denoted as NW (no water) and W (with water), respectively—to evaluate both the basic scCO<sub>2</sub> foaming capability and the influence of hot compressed water in

**Table 2** Foaming experimental conditions for time test (all with water at 45 MPa).

Test	P <sub>sat</sub> [MPa]	$H_2O$	$T_{sat}$ [°C]	t <sub>sat</sub> [min]
11	45	W	125	0
12	45	W	125	15
13	45	W	125	30
14	45	W	125	60
15	45	W	125	120
16	45	W	125	240

the same process. The saturation time ( $t_{sat}$ ) was fixed at 60 min for all pressure variation tests. In total, 10 runs were performed (Tests 1–10), covering saturation pressures from 15 MPa to 60 MPa. An additional run labeled X was conducted at 45 MPa (NW) using a slow gas purge for pressure release rather than the sudden depressurization, for comparison.

2.3.2.2. Time variation experiments. Table 2 lists the conditions for time variation tests, designed to understand how saturation duration influences foam properties under a pressure of 45 MPa. This choice was based on promising results from the pressure series. Six different hold times ( $t_{sat}=0$  min to 240 min) were assessed, all in the presence of water (W) at 125 °C.

2.3.2.3. Experimental procedure. The trials were executed as follows. The autoclave was initially filled with 10 g of PMMA pellets. Additionally, 10 g of water was added after the polymer in the experiments where water was tested. The mass of pellets and water was arbitrarily chosen to be the same. Although the autoclave does not have an impeller to mix both substances, the water was evenly distributed around the polymer. It can be visualized as water flowing down through the empty volume between randomly distributed pellets. Once the autoclave was filled with the polymer and water (if any), the system was sealed and heated to 125 °C ( $T_{sat}$ ). Once the autoclave reached the target temperature,  $CO_2$  was pumped in using the gas booster up to the desired saturation pressure ( $P_{sat}$ ). The polymer was held under these conditions for the set saturation time ( $t_{sat}$ ).

After saturation, the pneumatic ball valve was opened abruptly, causing instantaneous depressurization—on the order of milliseconds—and ejecting the foamed polymer into the expansion vessel. In addition to inducing a rapid pressure drop and short nucleation—growth window, this sudden expansion triggers the Joule—Thomson cooling effect, which quickly lowers the polymer temperature below its glass transition and effectively "freezes" the foam morphology, preventing cell coalescence or collapse [22].

The effectiveness of this one-step approach arises from three complementary features of the Siphon 1 system:

- High pressure-drop rate (PDR): Rapid decompression elevates nucleation rates and promotes fine cells.
- Above-T<sub>g</sub> expansion: Operating above the effective glass transition temperature ensures polymer chain mobility for cell growth.
- $\bullet$  Kinetic Ejection + Joule–Thomson Cooling: Expelling the polymer into a cooler vessel while simultaneously cooling it below  $T_g$  "locks in" the microcellular structure.

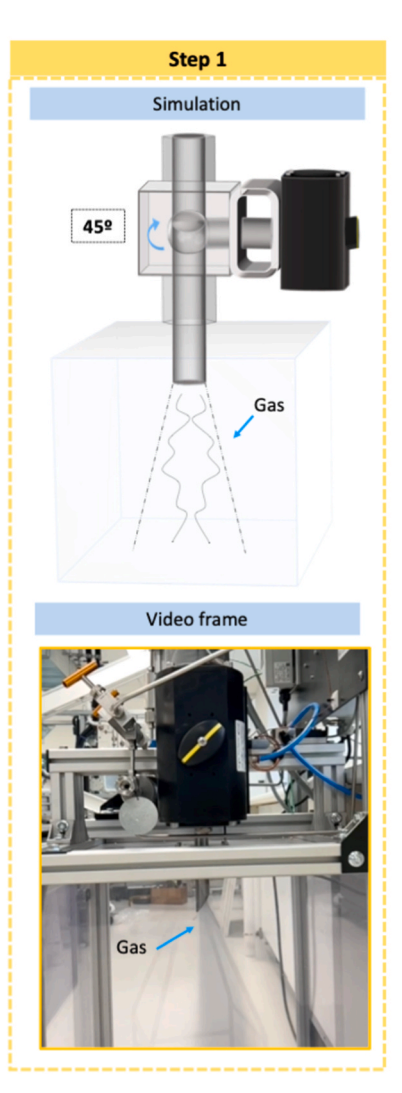
Subsequent sections present detailed analyses of the resulting foam structure and properties under both the pressure and time experimental series.

# 2.4. Analytical techniques

## 2.4.1. Particle size distribution of PMMA pellets

Particle size distribution of milled PMMA pellets were done in a Malvern Mastersizer 2000 Light Scattering equipment, from Malvern





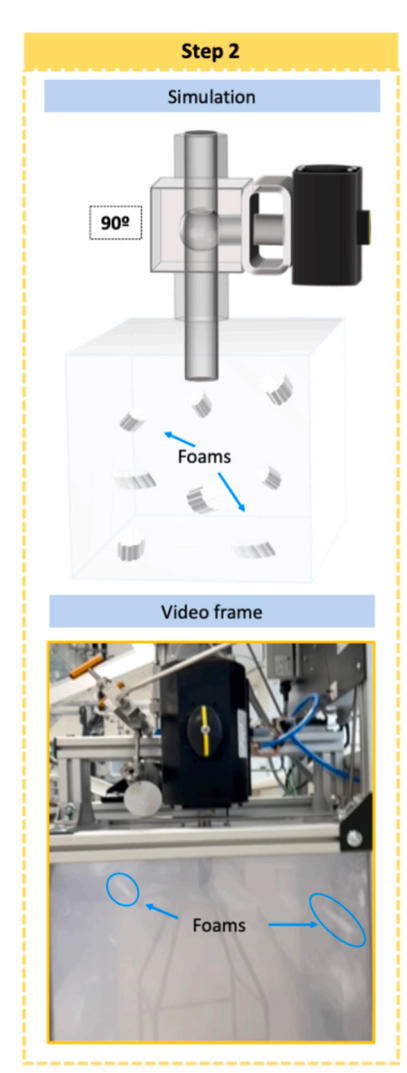


Fig. 3. Simulation of ball valve position sequence and actual image frame captures from video of the depressurization point are presented. Step 1 illustrates the release of the gas phase, while step 2 captures the ejection and expansion of foamed PMMA.

Instruments. The size was measured between 0.02  $\mu m$  and 2000  $\mu m$ .

#### 2.4.2. Scanning electron microscopy

The exterior of the foams and their cellular structure were analyzed by Scanning Electron Microscopy (SEM) (HITACHI FlexSEM 1000). Firstly, the samples were submerged in liquid nitrogen, to not modify the cellular structure, and then they were fractured. Afterward, a gold coating was applied to the surface with a sputter coater (BALZERS model SDC004, experimental conditions: 30 mA, 40 s and 25 nm thickness).

To characterize the cellular structure of the PMMA foams, the images were analyzed with software-based on ImageJ/FIJI, obtaining average cell size ( $\emptyset$ ) and cell density ( $N_v$ ).  $\emptyset$  was calculated as the mean value of the average diameter, considering more than 200 cells per samples.  $N_v$  was determined by Kumar's theoretical approximation as previously used in literature [41]. From these parameters, relative density ( $\rho_R$ ) and cell nucleation density ( $N_0$ ) was calculated by Eqs. 1 and 2. Finally, to evaluate the homogeneity of cell size distributions, standard deviation of cell size (SD) was calculated and SD/ $\emptyset$ , as a parameter of the width of these distributions, was determined [41].

$$N_0 = \frac{N_v}{\rho_R} \tag{1}$$

$$\rho_{R_{micro}} = 1 - \frac{N_{\nu}\pi \varnothing^3}{6} \tag{2}$$

# 2.4.3. Pressure drop rate

The pressure and temperature values were recorded during the experiments by a data acquisition software connected to the set-up. The data was captured every 0.06 s. The pressure sensor was located at the top of autoclave, measuring the pressure at the port opposite to the valve. Pressure drop in the immediate vicinity of the valve might be even higher. The temperature was measured at the top of autoclave, (saturation temperature), and also at the outlet of the autoclave, inside the expansion vessel. Pressure drop rates were calculated with the experimental data as the Eq. 3, with  $\Delta P$  denoting the pressure difference between starting and ending points of the depressurization and  $\Delta t$  representing the duration over which the pressure data was acquired.

$$PDR = \frac{\Delta P}{\Delta t} \tag{3}$$

## 2.4.4. Differential scanning calorimetry (DSC)

Thermal analysis was conducted on the raw material and foamed products to determine their glass transition temperature (Tg) using a Differential Scanning Calorimeter (DSC 3+) from Mettler Toledo (Mettler-Toledo S.A. E., L'Hospitalet de Llobregat, Barcelona, Spain), previously calibrated with indium. Approximately  $10\ mg$  -  $15\ mg$  samples were heated to  $160\ ^{\circ}\text{C}$  at the rate of  $10\ ^{\circ}\text{C}$  / min, followed by cooling to  $30\ ^{\circ}\text{C}$  at the same rate during the cooling cycle. The heating steps were

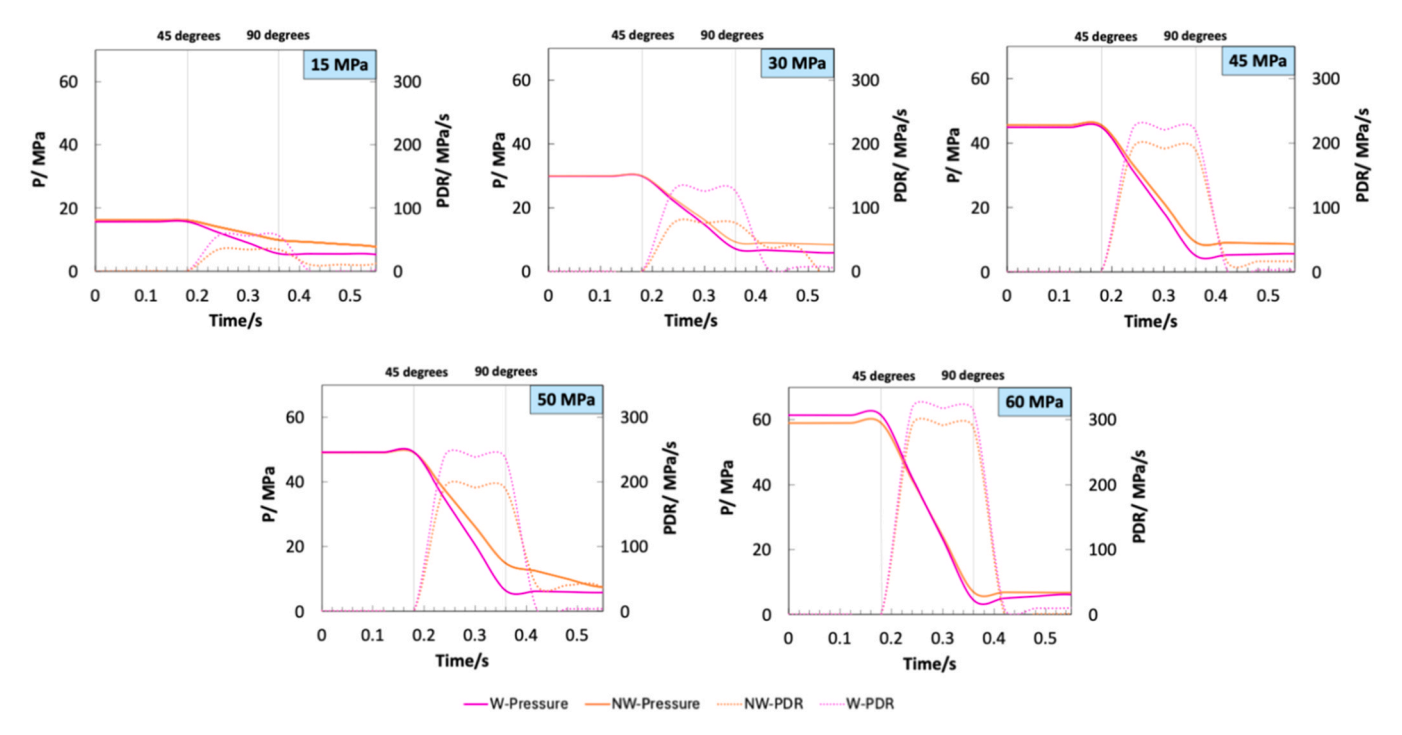


Fig. 4. The solid line represents the pressure profile, while the dotted line in secondary axis corresponds to the PDR profile, both recorded during the depressurization stage for each applied pressure.

repeated for a second scan. A nitrogen flow of  $60\,L$  / min was maintained to ensure an inert atmosphere, preventing mass gain due to oxidation. A low heating rate was chosen to minimize uncertainties in Tg measurement. The Tg was determined as the mid-point in the transition observed in the DSC thermogram.

#### 2.4.5. Density

The density of the foamed samples was determined using Archimedes' liquid displacement method. The liquid was ethanol. To achieve this, a density determination kit compatible with the AT261 Mettler-Toledo balance was utilized. The macroscopic relative density was calculated based on the measured density using Eq. 4.

$$\rho_{R_{macro}} = \frac{\rho_{Archimedes}}{\rho_{PMMA}} \tag{4}$$

#### 3. Results and discussion

# 3.1. Depressurization kinetics and process mechanism

The depressurization in this study is initiated by opening a pneumatic, full-port ball valve that seals the autoclave at the bottom (see Section 2.3.1). As the valve rotates, two distinct steps can be identified. In Step 1, when the valve is partially open (~45 °), CO<sub>2</sub> (and any dissolved or subcritical water) begins to escape, but the polymer remains in the vessel. In Step 2, the valve reaches 90 °, allowing the complete ejection of both residual fluid and foamed PMMA (see Fig. 3). This two-

stage mechanism typically completes in less than 0.5 s, underscoring how quickly the system discharges its content.

To quantify depressurization dynamics, pressure vs. time profiles (Fig. 4) were recorded for each test condition, enabling the calculation of pressure drop rates (PDR) (Table 3). Furthermore, the PDR values calculated for each data point (0.06 s interval) were represented in Fig. 4 by the dotted profile. When no water (NW) is present, the system displays a two-step pressure drop aligned with the valve rotation sequence. In this case, both PDR1 (from autoclave pressure to partial opening) and PDR2 (from partial opening to atmospheric pressure) increase with higher saturation pressure. Notably, PDR1 is consistently larger than PDR2, indicating a more abrupt drop during the initial release of CO<sub>2</sub>.

In contrast, the water-assisted (W) runs often appear as a single-step release, with most of the pressure lost before the valve even reaches 90  $^\circ$ . Moreover, the pressure-drop rates obtained in the water procedure are higher than those recorded in the experiments conducted without water. Because hot compressed water flashes into steam upon depressurization, it contributes additional vapor volume compared to  $\text{CO}_2$  alone, leading to higher PDR values. The "PDR gain" represents how much the PDR is increased by adding water to the system. At elevated pressures, the mechanical limits of the pneumatic valve may curtail further gains in depressurization speed. Overall, these data confirm that adding water (and thus generating in situ steam) significantly intensifies depressurization from temperatures above 100  $^\circ\text{C}$ .

All experiments were conducted at 125 °C, ensuring that PMMA stayed above its effective glass transition temperature when the valve was opened. In this rubbery state, the polymer undergoes rapid

Table 3
Pressure profile, pressure drop rates and PDR gain for each condition. P<sub>sat,i</sub>: initial saturation pressure; P<sub>sat,f</sub>: final saturation pressure.

		NW			W		
P <sub>sat, t</sub> [MPa]	P <sub>sat,I</sub> [MPa]	P <sub>sat,f</sub> [MPa]	PDR [MPa/s]	P <sub>sat, I</sub> [MPa]	P <sub>sat, f</sub> [MPa]	PDR [MPa/s]	PDR Gain [MPa / s]
15	16.1	9.9	34.4	15.7	5.6	56.1	21.7
30	23.2	9.5	76.1	29.8	7.1	126.1	50.0
45	44.6	10.2	191.0	44.9	5.1	221.1	30.1
50	49.1	14.8	190.5	49.3	6.4	238.3	47.8
60	59.0	6.9	289.4	61.3	4.4	316.1	26.7

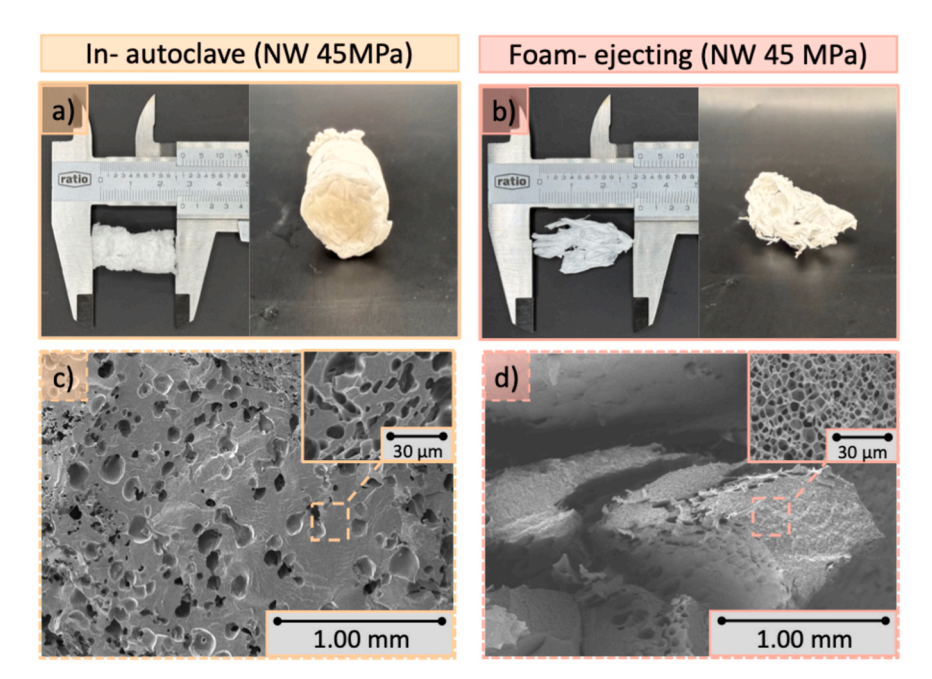


**Fig. 5.** Comparison of samples produced by the two pressure release techniques; a) Foamed product appearance from in-autoclave depressurization, scale in cm; b) Foamed product from test 3 through foam-ejecting technique, scale in cm; c) Two micrographs magnifications (x50 and x1.50 k) of the product from in-autoclave technique; d) Two different magnifications (x50 and x1.50 k) from test 3 foamed product.

expansion as  $CO_2$  (and water) transitions from supercritical fluid to gas or steam. Simultaneously, the Joule–Thomson cooling that accompanies sudden pressure drops rapidly solidifies the foam structure once enough gas has escaped and the local temperature falls below  $T_g$ . Such quasi-instantaneous cooling locks in the cellular morphology, preventing collapse. This high-PDR, one-step expansion is central to forming microcellular foams, as it simultaneously maximizes nucleation while minimizing the time available for bubbles to coalesce. In addition, the pressure release was designed to be carried out through a full-port ball valve, allowing the polymer to exit the saturation vessel abruptly and giving kinetic energy to the polymer while cooling and expanding. Consequently, the obtained products showed elongated and fibrous shapes, and their cellular structures were composed of microcellular foamed layers, as will be discussed in the following sections.

To further highlight the kinetic importance of this approach, an additional test was performed at 45 MPa, where the polymer remained in the autoclave during a slower depressurization via the purge valve. Here, the PDR only reached 65 MPa / s, compared to > 150 MPa / s under normal (foam-ejecting) conditions. As Fig. 5 shows, the inautoclave sample formed a bulkier, coarser foam that lost much of its homogeneous microcellular character. Because the temperature in the autoclave remained near 125 °C for a longer time during the slower release, partial collapse likely occurred before the sample cooled below  $T_{\rm g}.$  It should be considered that the cooling due to the Joule-Thompson effect is compensated by the thermal energy given by the autoclave metal, valves, and environment. By contrast, materials ejected through the ball valve developed multi-fibrillar, finer pores, with pore sizes up to an order of magnitude smaller.

These results show that one-step saturation and high-rate depressurization—particularly in the presence of subcritical water—strongly influence both foam ejection and final morphology. This technique allows the production of PMMA multilayer monomaterial foams. This is particularly important when the polymer is decompressed at temperatures above the effective glass transition temperature [29]. The key factors at play are:

 Stepwise valve opening: Governs the initial gas release versus full polymer ejection.

- Steam generation: In water-assisted runs, steam explosively enhances the PDR, promoting finer-cell foams.
- Above-T<sub>g</sub> foaming + rapid cooling: The polymer's rubbery state enables rapid bubble growth, and subsequent Joule-Thomson cooling freezes the structure.
- Kinetic vs. slow pressure release: Using a full-port ball valve enables abrupt polymer ejection, imparting kinetic energy during expansion and yielding elongated, layered foams. In contrast, slower purges within the autoclave produce bulkier or partially collapsed structures.

In the following sections, these mechanisms are linked to the microcellular morphologies observed across various pressures, foaming times, and pellet sizes.

#### 3.2. Macroscopic structure: multi-layer foam material

To gain insight into the overall morphology, SEM images were captured at low magnification (x50) for each experimental pressure and water condition. Those images are shown in a matrix in Fig. 6. Each row in the figure corresponds to a saturation pressure ranging from 15 MPa to 60 MPa, while the columns differentiate no-water (NW) versus water-assisted (W) runs. Across all tests, the autoclave temperature and saturation time were fixed at 125  $^{\circ}\text{C}$  and 60 min, respectively.

After foaming, each condition produced numerous lightweight pieces of PMMA (typically  $\sim\!100$  per run). The original transparent pellets became opaque upon foaming, reflecting the creation of gas-filled cells within the polymer matrix. Remarkably, most samples presented layered foam structures with varied thicknesses and shapes—a phenomenon not commonly reported in conventional microcellular foaming [42–44].

These layer-over-layer features appear especially pronounced at lower pressures (15 MPa - 30 MPa), where distinct heterogeneous layers become evident, reflected by variations in pore sizes between pellets within the same run (Fig. 6a, b, f, g). By 45 MPa, a more uniform porosity (Fig. 6c, h) is achieved, and at 50 MPa - 60 MPa (Fig. 6d, e, i, j), fully saturated and homogenized layers predominate, yielding consistent microcellular foam structures.

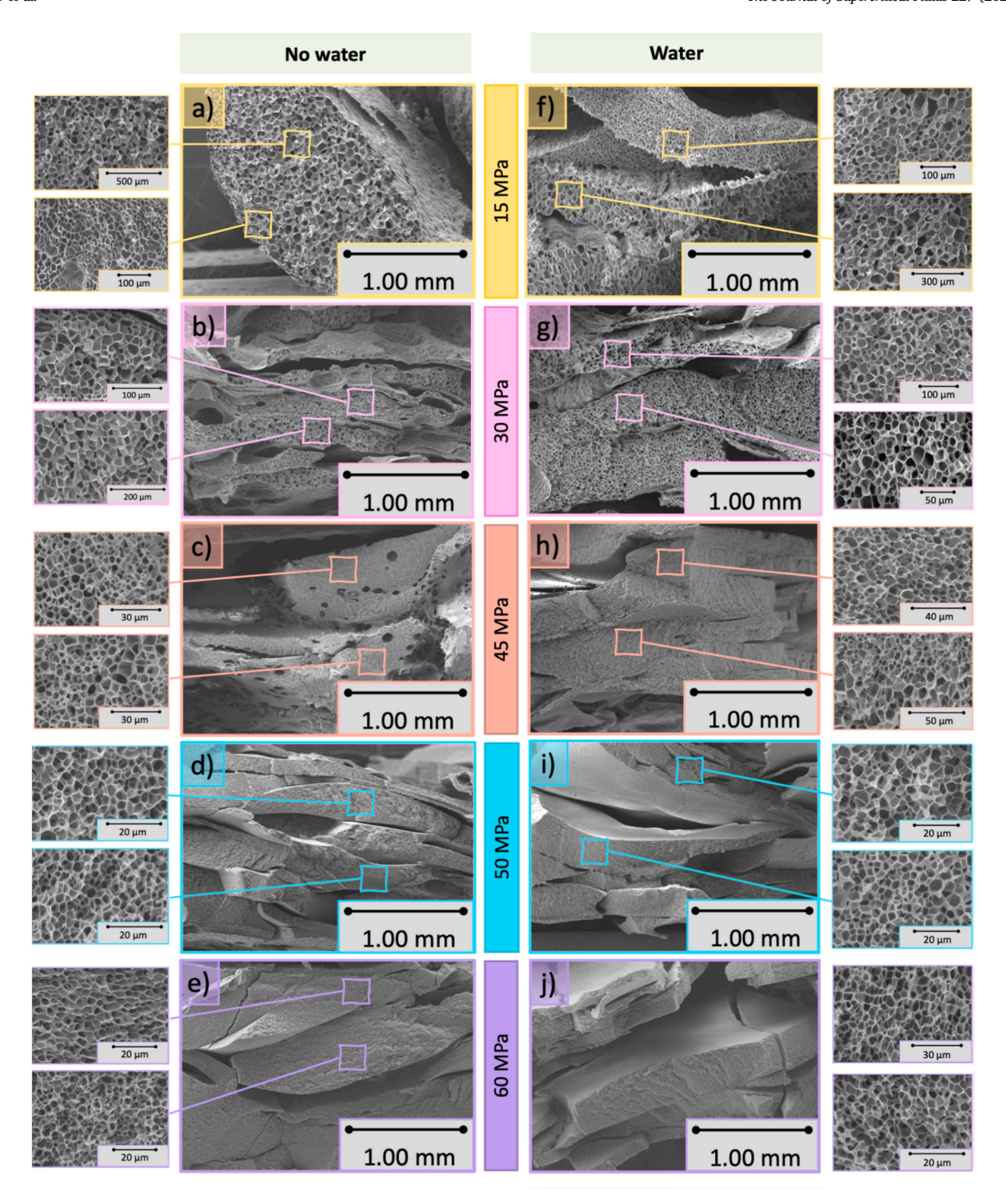


Fig. 6. SEM images at different pressures and water conditions. a) NW- 15 MPa; b) NW- 30 MPa; c) NW- 45 MPa; d) NW- 50 MPa; e) NW- 60 MPa; f) W-15 MPa; g) W-30 MPa; h) W-45 MPa; i) W-50 MPa; j) W- 60 MPa. Magnification of x50, x100, x150, x500, x1.00 k, 1.5 k, 2.00 k, 3.00 k to 1.00 mm, 500  $\mu$ m, 300  $\mu$ m, 30  $\mu$ m, 30  $\mu$ m, 20  $\mu$ m and 10 $\mu$ m respectively.

These trends can be tied to the particle size distribution (300  $\mu m$  - 2000  $\mu m$ ; see Section 3.1) of the milled PMMA. This suggests that different sub-populations of pellets absorbed varying amounts of  $CO_2$ , so each individual pellet could saturate to a different degree within the same batch. Larger pores typically arise from lower gas dissolution, while finer pores indicate higher dissolution. As such, at 15 MPa – 30 MPa the smaller pellets may foam readily, while larger pellets only partially saturate, creating layer-to-layer differences in pore sizes. In contrast, higher pressures ( $\geq$ 45 MPa) facilitate sufficient  $CO_2$  uptake across the entire pellet size distribution, producing uniform pore

morphologies within each layer. Consequently, the final foamed product assembles as stacked layers—each originating from a distinct pellet—rather than forming a single coherent piece of polymer.

Further evidence of multilayer morphology includes voids between layers and irregular pores at the boundaries, indicating discrete interfaces. Despite this layering, the one-step saturation and rapid depressurization prevented formation of a dense "skin" typically seen in gas-dissolution foams [45]. By operating above  $T_{g,eff}$  (enhanced by  $CO_2$  plasticization) and depressurizing abruptly, the system maintained sufficient gas concentration at the polymer surface for complete nucleation

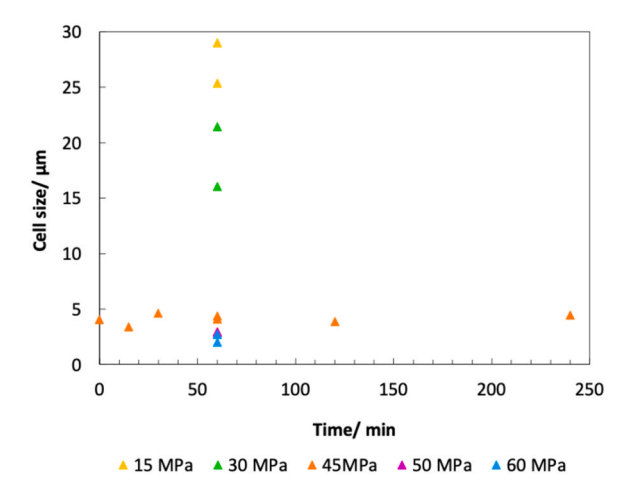


Fig. 7. Cells size plot as a function of time for each experimental pressure condition.

throughout the sample [46].

Therefore, the multilayer monomaterial architecture—though somewhat unexpected—offers an extra degree of structural control stemming from particle size distribution and the one-step foaming protocol. Moreover, elevated pressures not only boost the total CO2 content in the polymer (thus reducing pore sizes) but also accelerate saturation kinetics, leading to more uniform pore sizes across pellets of different dimensions. Another notable finding is that individual pellets display consistent porosity—whether the cells are relatively small (higher dissolved CO<sub>2</sub>) or large (lower dissolved CO<sub>2</sub>)—indicating that CO<sub>2</sub> distributes evenly in the polymer once PMMA is above T<sub>g</sub>. In this "high-mobility" regime, faster gas diffusion enables homogeneous cell nucleation, even at lower absolute CO2 concentrations. As a result, under higher-pressure conditions, the multilayer architecture becomes more coherent, reflecting a closer match in gas loading across various pellet sizes. The subsequent sections explore how this multilayer structure evolves under different pressures, saturation times, and the presence or absence of subcritical water.

Controlling the pore size and the thickness of the layers will be a key feature for developing novel materials. The pore size is well understood and mainly influenced by saturation pressure, temperature and time and PDR. On the other hand, the control over layer thickness seems to be more complicated. However, it can be speculated that this will depend, at least of the: number of pellets in the autoclave, size of the pellets, saturation temperature and pressure, amount of water, PDR and speed of ejection from the autoclave (kinetic energy).

#### 3.3. Influence of saturation time

To assess how saturation time influences foam morphology, pore

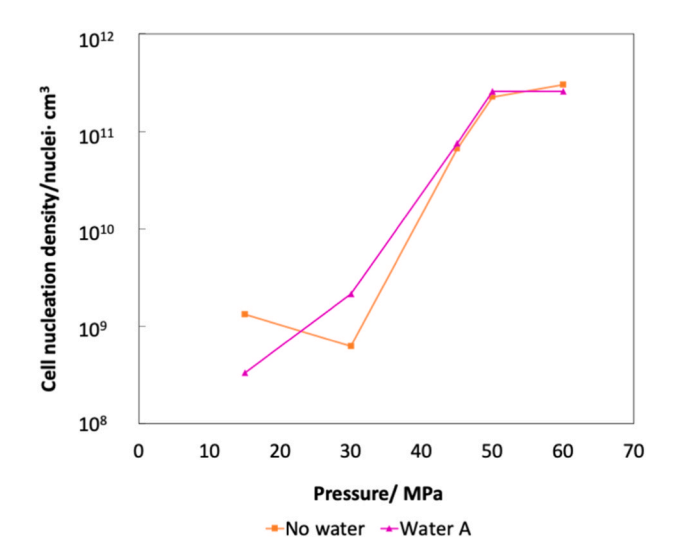


Fig. 9. Average of cell nucleation density as a function of pressure.

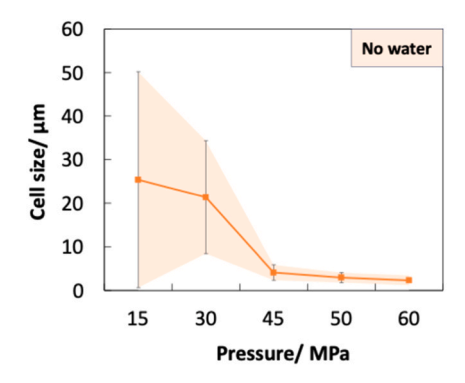
sizes were evaluated over a range of  $0 \, \text{min}$  –240 min at several pressures. Fig. 7 summarizes the resulting cell size trends as a function of time for each pressure considered.

Surprisingly, cell size remained nearly constant across the entire time window—regardless of whether the samples were left to saturate for a few minutes or up to four hours. This contrasts sharply with conventional two-step foaming approaches, where lengthy saturation at sub-Tg temperatures often plays a critical role in determining cell structure. In the present one-step method, operating above  $T_{g,eff}$  significantly enhances  $CO_2$  diffusion into the polymer matrix, allowing rapid gas dissolution within minutes or even seconds. Consequently, time is not a limiting factor in this one-step protocol, as extended holding meaning up to 240 min do not further reduce pore size or increase uniformity. Instead, pressure (along the associated pressure drop rate) and water-assisted condition emerge as the dominant factors governing pore nucleation and growth, overshadowing any benefit of extended well times.

These observations underscore the feasibility of producing microcellular PMMA within very short processing times. Such findings offer a notable process intensification advantage, as shorter saturation steps translate into lower energy usage and higher throughput.

# 3.4. Influence of pressure

An overarching observation is that cell size decreases as saturation pressure ( $P_{sat}$ ) increases (Fig. 8). Because both time and temperature (60 min, 125 °C) were held constant, it is straightforward to isolate how pressure influences the final foam morphology. SEM micrographs confirm that micrometric cells form in all foams, with a clear downward



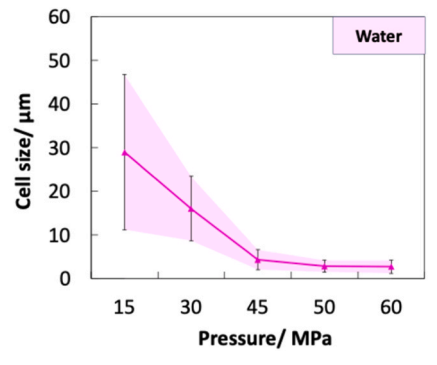


Fig. 8. Cell size and their error bars analysis as a function of pressure for each experimental condition.

shift in cell size as Psat rises.

Under increased pressure—and therefore heightened solubility of CO<sub>2</sub>—a greater number of nuclei can form, ultimately leading to smaller pores [14]. The depressurization rate (PDR) also grows with pressure (Section 3.1), limiting bubble coalescence time and promoting finer cell structures. Hence, pressure and PDR are intrinsically linked in this one-step process and must be considered jointly.

Additionally, cell nucleation density increases with pressure (Fig. 9), especially at 45 MPa and above.

Meanwhile, a measure of cell-size homogeneity (SD/Ø, see Table S1) also indicates that foams at low pressures (15 MPa – 30 MPa) are relatively non-uniform, whereas 60 MPa runs can reach SD/Ø  $\approx 0.5$  [28, 43]. These results reinforce the strong dependence of foam quality on saturation pressure, as higher pressures (and associated higher PDR) drive the system toward smaller, more uniform pores. On the other hand, the results at pressures below 30 MPa suggest that the use of water reduces the pore size dispersion (see SD/Ø, see Table S1). This effect becomes less relevant at pressures above 45 MPa. The velocity of CO2 diffusion into the PMMA matrix will depend mainly on the diffusion coefficient and the CO2 concentration difference (driving force) between the gas and the polymer matrix. As the CO2 concentration depends on the gas phase pressure, a higher pressure becomes a higher driving force and hence a higher CO2 velocity of polymer saturation.

Overall, the pressure effect manifests in two ways. A higher pressure enhances the  $CO_2$  solubility leading to higher nucleation density and smaller cell sizes; and a faster depressurization (higher PDR) suppresses coalescence. Together, these factors ensure that above  $\sim\!45$  MPa, the PMMA foam transitions from heterogeneous, layered morphologies to largely homogeneous microcellular structures.

#### 3.5. Role of water

Experiments involving subcritical water (W) exhibit a sharper decline in pore size relative to their no-water (NW) counterparts (Fig. 8). From this figure, the error bars, representing the standard deviations, clearly indicate that experiments conducted in water exhibit a greater uniformity in cell sizes. Although the macroscopic appearance of W and NW samples may not differ substantially—especially at higher pressures—closer inspection reveals fewer defects and more homogeneous cellular structures in water-assisted foams. This aligns with the notion that PMMA's hydrophobicity largely prevents water from entering the polymer directly [40]; instead, water serves as a plasticizing agent that lowers Tg, promotes a more rubbery polymer state, and thus allows more homogeneous pore formation [47]. This reduction leads to a more fluid polymer state during processing, which in turn minimizes structural defects and enhances the overall quality of the material.

Steam-assisted runs show higher nucleation densities (Fig. 9), confirming that a faster PDR favors nucleation over cell growth [14,29,48,49]. This behavior confirms that steam-assisted foaming with higher PDR values can lead to increased nucleation and faster blockage of the cellular structure due to vitrification of the samples. This leads to gas being used for nucleation rather than cell growth, resulting in reduced coalescence phenomena and smaller pore sizes.

Additionally, to quantify these differences, Archimedes density and the resulting expansion ratios were measured for select samples (Table S2 – Supporting Information, Fig. 10). These density measurements are performed on several portions of the foam obtained from each experiment. Therefore, it is considered the macroscopic density of the PMMA foams.

As expected, NW samples show a steady drop in relative density with rising pressure, confirming that higher  $P_{sat}$  enhances  $CO_2$  solubility. Water-assisted (W) samples follow a similar general trend but exhibit slightly lower densities at lower pressures (15 MPa - 30 MPa), suggesting that steam-driven nucleation effectively boosts foam expansion at moderate pressures.

Moreover, NW samples typically exhibit a gradual, predictable

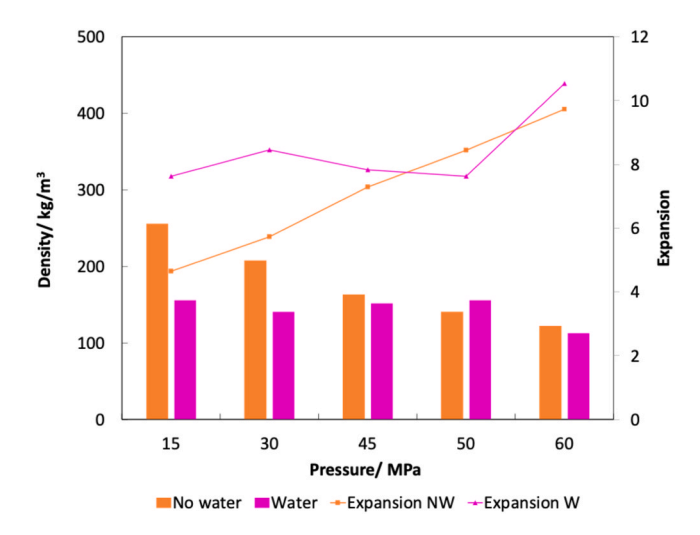


**Fig. 10.** Archimedes density in the graph plot and expansion in the line plot, measured for both water condition and each experimental pressure.

increase in expansion with increasing pressure, while the W samples show greater scatter but still achieve larger expansions on average. This underscores water's ability to amplify  $CO_2$  foaming at elevated pressures, effectively serving as an auxiliary blowing agent to improve mass transfer and accelerate nucleation.

Table S2 also indicates that  $\Delta T_g$  (the shift in glass transition relative to precursor PMMA) depends on pressure and processing conditions, with water-assisted samples often showing greater shifts. Lower relative densities typically coincide with higher  $\Delta T_g$ , suggesting that porosity—in combination with residual  $CO_2$  and the plasticizing effect of water—modulates the polymer's thermal behavior. In essence, higher foaming efficiency (driven by steam and  $CO_2$ ) can lead to more pronounced changes in the polymer's glass transition, indicating deeper fluid—polymer interactions.

Overall, these results confirm that while subcritical water does not penetrate PMMA directly, it provides multiple benefits in conjunction with  $scCO_2$ . The steam explosion increases PDR and nucleation, yielding finer cells and fewer structural defects. The plasticization lowers  $T_g$ , promoting faster gas diffusion and more uniform foaming. The higher PDR (especially at moderate-to-high pressures) promoted by water helps reduce foam density and boost polymer expansion.

Consequently, one-step saturation and foaming in the presence of water can achieve cell sizes below 3  $\mu m$ , while retaining a largely homogeneous structure. Water thus acts as an auxiliary blowing agent, enhancing the basic CO<sub>2</sub> process rather than inhibiting it.

Therefore, employing one-step for saturation and foaming process makes it feasible to obtain PMMA foams with cell sizes below 3  $\mu m$  for both no water and water experiments at the maximum pressure of 60 MPa. The control of homogeneity becomes achievable from 45 MPa onwards.

## 3.6. Pellet sizes and shape's influence in cellular structures

To investigate whether pellet size and shape affect the final foam morphology, two additional experiments were performed at 30 MPa using non-milled PMMA pellets of well-defined, cylindrical dimensions. One set had pellets measuring 2.35 mm in diameter  $\times$  3 mm in length (denoted "2 mm" pellets), and the other set had pellets 1 mm in diameter  $\times$  2.5 mm in length ("1 mm" pellets). As shown in Fig. 11, the resulting foams maintained the layered appearance but exhibited thicker, more homogeneous layers than those formed from milled pellets.

A particularly striking outcome of this process is the emergence of multilayer structures in which each individual layer displays a high

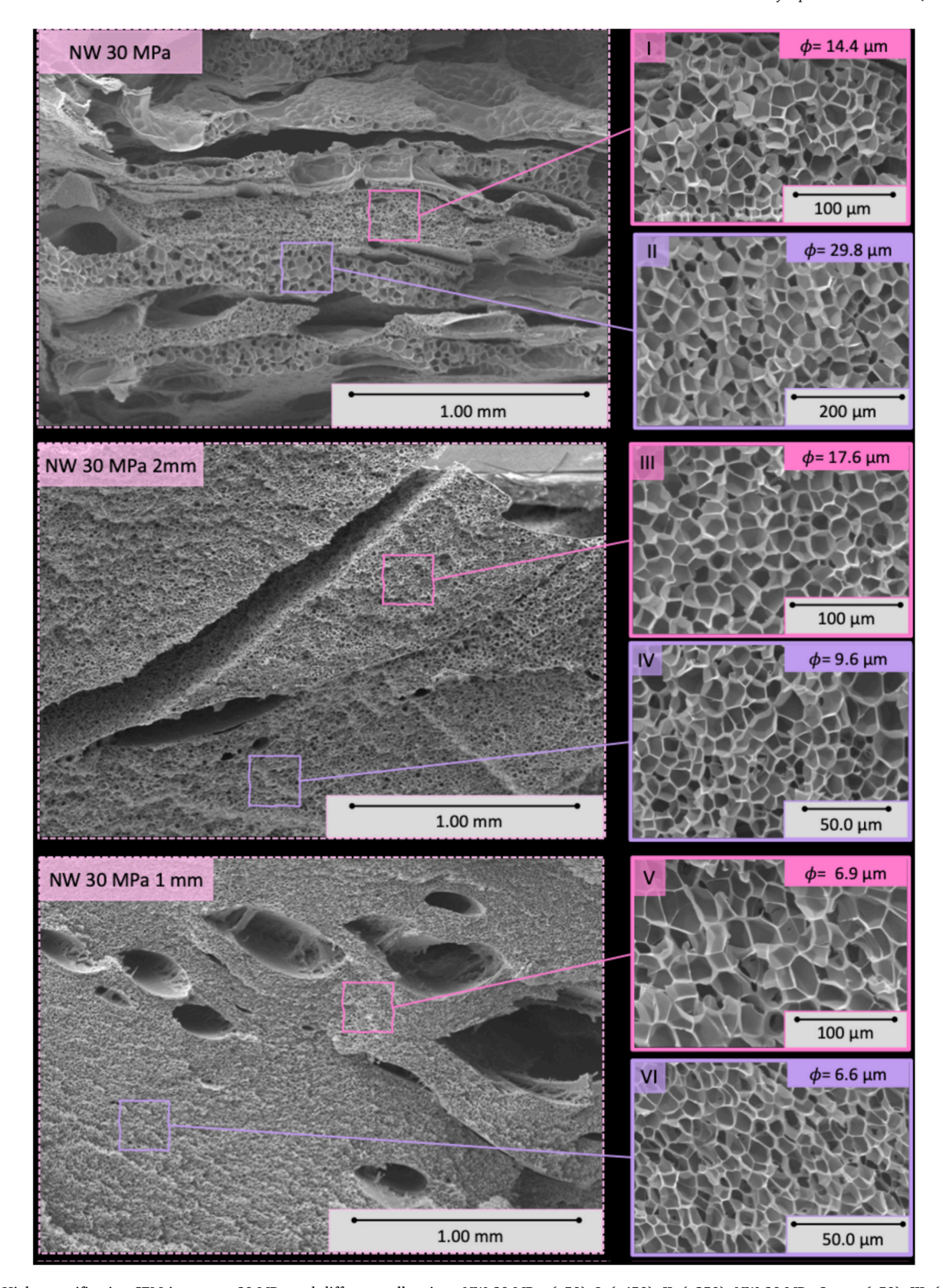


Fig. 11. High magnification SEM images at 30 MPa and different pellet sizes. NW 30 MPa: (x50); I: (x450); II: (x250); NW 30 MPa 2 mm: (x50); III: (x500); IV: (x750); NW 30 MPa 1 mm: (x50); V: (x1.50 k); VI: (x1.00 k).

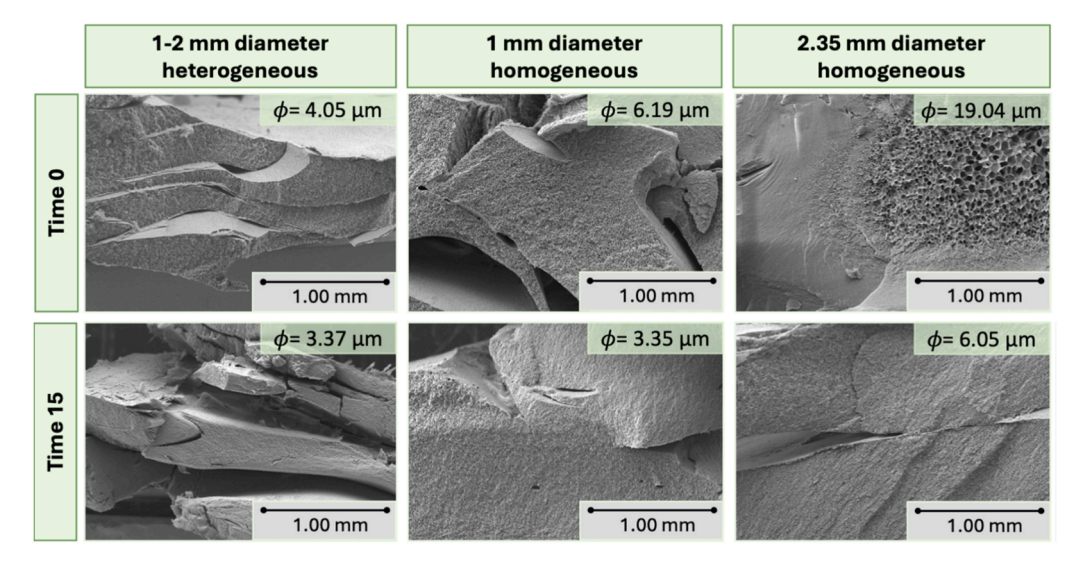


Fig. 12. High magnification SEM images (x50) at 45 MPa and different pellet sizes and saturation times.

degree of internal homogeneity—yet differs from its neighboring layers in terms of pore size. This suggests that, even with relatively short saturation times, each pellet acquire enough internal  $CO_2$  to enable uniform nucleation, even if the overall saturation level varies among pellet sizes. The resulting layered architecture, composed of structurally consistent but morphologically distinct domains, is a novel characteristic of this process. It suggests that saturation kinetics are fast enough in the rubbery PMMA matrix to enable localized, homogeneous foaming, even when global saturation is incomplete. This behavior not only reinforces the robustness of the one-step method but also opens opportunities for producing functionally graded materials in a single batch.

Image analysis (via ImageJ/Fiji) revealed pore sizes ranging from 29.8  $\mu m$  to 14.4  $\mu m$  for the milled 2 mm control, whereas non-milled 2 mm pellets yielded smaller (17.6  $\mu m$  –9.6  $\mu m$ ) but still heterogeneous cells at 30 MPa. By contrast, 1 mm non-milled pellets foamed into structures with pore sizes down to 7  $\mu m$ , displaying near-complete homogeneity at the same pressure. These comparisons confirm that uniform pellet geometry can enhance saturation efficiency, but achieving fully homogeneous foams may still require higher pressures or other process optimizations.

To further explore these size-dependent effects, additional runs were conducted at 45 MPa,  $125\,^{\circ}$ C, and various saturation times. Fig.  $12\,$  illustrates the foams produced from 2.35 mm pellets, 1 mm pellets, and milled pellets (1 mm – 2 mm range). At time zero, all samples showed some degree of foaming; however, the 2.35 mm pellets did not reach complete saturation within the shortest time. By 15 min of saturation, all pellet sizes achieve a comparatively homogeneous cellular structure, with cell sizes continuing to decrease slightly in the smaller pellets. Beyond this point, pore sizes appeared to stabilize, suggesting that any initial size-driven differences in saturation or cell nucleation were largely mitigated by additional soak time.

These results underscore two main conclusions. First, pellet geometry (i.e., diameter and length) strongly influences early-stage saturation and hence initial pore formation. Larger pellets require more time to attain uniform  $\rm CO_2$  distribution, leading to transitional heterogeneities in pore size. Second, once saturation proceeds for an adequate duration—particularly under higher pressures—the PMMA rubbery state promotes rapid gas diffusion, reducing size-driven disparities and yielding stable, uniform foam morphologies across the batch. Consequently, while pellet size does shape foam microstructure at very short times (e.g., 0 min), the overall influence diminishes or disappears with modest increases in saturation time.

#### 4. Conclusions

This work introduces a novel steam-assisted, one-step supercritical  $CO_2$  foaming process that enables the rapid production of multilayer polymethylmethacrylate (PMMA) foams with unprecedented structural development. The innovation lies not only in the process—which departs fundamentally from conventional gas dissolution routes—but also in the outcome: the spontaneous formation of integrated multilayer foams, each layer characterized by a distinct pore size. These materials, with tunable architectures and gradient porosity, offer new opportunities for advanced polymer foams tailored for specific functional or mechanical demands.

This work introduces a foaming process entirely above the polymer's glass transition temperature. Operating at  $125\,^{\circ}\text{C}$ , the process drastically reduces saturation times to single digit minutes while maintaining excellent control over cell nucleation and growth. The introduction of subcritical water, which flashes into steam upon depressurization, significantly raises the pressure drop rate (up to 40 % faster), promoting finer (2.3  $\mu\text{m}$ ), more homogeneous cellular structures and enabling efficient foaming even at lower pressures.

A particularly distinctive outcome is the formation of multilayer monomaterial foams, where partially saturated PMMA pellets fuse into integrated structures with spatially distinct porosities. This architecture emerges naturally from the short saturation times and the enhanced  $CO_2$  mobility in the rubbery polymer state. The resulting multilayered foams offer a new strategy for engineering gradient materials, where each layer can be tailored for specific mechanical, thermal, or acoustic functions.

Steam-assisted foaming not only improves foam uniformity and reduces defects but also provides an energy-efficient pathway to scalable, rapid polymer processing. Altogether, the combination of rapid saturation, steam-enhanced expansion, and multilayer structural design represents a significant advancement toward the sustainable manufacturing of high-performance polymer foams with customizable microstructures, targeting next-generation applications in lightweight engineering, energy absorption, and functional insulation.

#### CRediT authorship contribution statement

**Aránzazu Redondo:** Writing – review & editing, Writing – original draft, Visualization, Methodology, Investigation, Formal analysis, Data curation, Conceptualization. **Michel Simard:** Writing – review & editing, Supervision, Formal analysis, Conceptualization. **de-León Judith Martín:** Writing – review & editing, Validation, Supervision, Formal analysis, Conceptualization. **Danilo Cantero:** Writing – review &

editing, Writing – original draft, Visualization, Supervision, Investigation, Funding acquisition, Formal analysis, Conceptualization.

#### **Declaration of Competing Interest**

The authors declare that they have no known competing financial interests or personal relationships that could have appeared to influence the work reported in this paper.

#### Acknowledgements

The authors express their gratitude to the Agencia Estatal de Investigación for the financial support provided PID2020-119249RA-I00. This work received backing from the Regional Government of Castilla y León (Spain) and the EU-FEDER program (CLU-2029-04). The program from Ministerio de Ciencia e Innovación, EU NextGenerationEU/PRTR program, Regional Government of Castilla y León, and EU-FEDER: "Plan Tractor En Materiales Avanzados Enfocado A Los Sectores Industriales Claves En Castilla Y León: Agroalimentario, Transporte, Energía Y Construcción (MA2TEC)" are gratefully acknowledged. The authors also wish to acknowledge the Cellular Materials Laboratory (CellMat) at University of Valladolid (Spain) for supplying PMMA Plexiglass® 7 N in pellet form. The authors thank Paula García for her technical and lab support. Danilo Cantero is funded by the Spanish Ministry of Science, Innovation and Universities ("Beatriz Galindo" fellowship BEAGAL18/00247). Aranzazu Redondo is funded by the University of Valladolid predoctoral grant 2022.

#### Appendix A. Supporting information

Supplementary data associated with this article can be found in the online version at doi:10.1016/j.supflu.2025.106746.

# **Data Availability**

Data will be made available on request.

#### References

- [1] V. Kumar, N.P. Suh, A process for making microcellular thermoplastic parts, Polym. Eng. Sci. 30 (1990).
- [2] D. Miller, P. Chatchaisucha, V. Kumar, Microcellular and nanocellular solid-state polyetherimide (PEI) foams using sub-critical carbon dioxide I. Processing and structure, Polym. (Guildf.) 50 (2009) 5576–5584, https://doi.org/10.1016/j. polymer.2009.09.020.
- [3] J.A.R. Ruiz, P. Viot, M. Dumon, Microcellular foaming of polymethylmethacrylate in a batch supercritical CO2 process: effect of microstructure on compression behavior, J. Appl. Polym. Sci. 118 (2010) 320–331, https://doi.org/10.1002/ app.32351.
- [4] J.E. Martini-Vvedensky, N.P. Suh, F. Church, F.A. Waldman, Microcellular Closed Cell Foams and their Method of Manufacture, 1984.
- [5] J.E.W.V. Kumar, A process to produce microcellular PVC, Int. Polym. Process. 1 (1993).
- [6] I. Sánchez-Calderón, V. Bernardo, J. Martín-de-León, M.Á. Rodríguez-Pérez, Novel approach based on autoclave bead foaming to produce expanded polycarbonate (EPC) bead foams with microcellular structure and controlled crystallinity, Mater. Des. 212 (2021), https://doi.org/10.1016/j.matdes.2021.110200.
- [7] J.E. Weller, V. Kumar, Solid-state microcellular polycarbonate foams. I. the steadystate process space using subcritical carbon dioxide, Polym. Eng. Sci. 50 (2010) 2160–2169, https://doi.org/10.1002/pen.21736.
- [8] T.J. Yoon, W. Kong, D.E. Kwon, B.K. Park, W.II Lee, Y.W. Lee, Preparation of solid-state micro- and nanocellular acrylonitrile-butadiene-styrene (ABS) foams using sub- and supercritical CO2 as blowing agents, J. Supercrit. Fluids 124 (2017) 30–37, https://doi.org/10.1016/j.supflu.2017.01.004.
- [9] Y. Han, Z. Yu, T. Zhang, X. Zhang, A.D. Phule, Z.X. Zhang, S.H. Jang, Fabrication of Open-Cell microcellular acrylonitrile butadiene styrene composite foams with enhanced electrical conductivity and high-performance electromagnetic interference shielding, Adv. Eng. Mater. 24 (2022), https://doi.org/10.1002/ adem\_202101020.
- [10] D.F. Baldwin, N.P. Suh, A microcellular processing study of poly(ethylene terephthalate) in the amorphous and semicrystalline states. Part I: microcell nucleation, Polym. Eng. Sci. 36 (1996).

- [11] L. Sorrentino, E. Di Maio, S. Iannace, Poly(ethylene terephthalate) foams: correlation between the polymer properties and the foaming process, J. Appl. Polym. Sci. 116 (2010) 27–35, https://doi.org/10.1002/app.31427.
- [12] R. Guan, B. Wang, D. Lu, Preparation of microcellular poly(ethylene terephthalate) and its properties, Appl. Polym. Sci. 88 (2003) 1956–1962.
- [13] Q. Ren, X. Zhu, W. Li, M. Wu, S. Cui, Y. Ling, X. Ma, G. Wang, L. Wang, W. Zheng, Fabrication of super-hydrophilic and highly open-porous poly (lactic acid) scaffolds using supercritical carbon dioxide foaming, Int J. Biol. Macromol. 205 (2022) 740–748, https://doi.org/10.1016/j.ijbiomac.2022.03.107.
- [14] I. Tsivintzelis, A.G. Angelopoulou, C. Panayiotou, Foaming of polymers with supercritical CO2: an experimental and theoretical study, Polymer 48 (2007) 5928–5939, https://doi.org/10.1016/j.polymer.2007.08.004.
- [15] E. Reverchon, S. Cardea, Production of controlled polymeric foams by supercritical CO2, J. Supercrit. Fluids 40 (2007) 144–152, https://doi.org/10.1016/j. supflu.2006.04.013.
- [16] W. Qiang, D. dong Hu, T. Liu, L. Zhao, Strategy to control CO 2 diffusion in polystyrene microcellular foaming via CO 2 -philic additives, J. Supercrit. Fluids 147 (2019) 329–337, https://doi.org/10.1016/j.supflu.2019.01.002.
- [17] J.A. Reglero Ruiz, M. Dumon, J. Pinto, M.A. Rodriguez-Pérez, Low-density nanocellular foams produced by high-pressure carbon dioxide, Macromol. Mater. Eng. 296 (2011) 752–759, https://doi.org/10.1002/mame.201000346.
- [18] K.Y. Kim, S.L. Kang, H.-Y. Kwak, Generation of microcellular foams by supercritical carbon dioxide in a PMMA compound, Inter. Polym. Process. XXIII 1 (2008). (www.hanser-elibrary.com).
- [19] V. Bernardo, J. Martin-de Leon, M. Rodriguez-Perez, Production of PMMA-based nanocellular polymers using low demanding saturation conditions, Mater. Lett. 255 (2019), https://doi.org/10.1016/j.matlet.2019.126551.
- [20] K. Güzel, J.-C. Zarges, H.-P. Heim, Effects of the cellular morphology on fatigue deformation mechanisms of physically foamed polycarbonate (in:), SPE Foams (2023).
- [21] C.B. Park, D.F. Baldwin, N.P. Suh, Effect of the pressure drop rate on cell nucleation in continuous processing of microcellular polymers, Polym. Eng. Sci. 35 (1995).
- [22] R. Li, N. Ye, V. Shaayegan, T. Fang, Experimental measurement of CO2 diffusion in PMMA and its effect on microcellular foaming, J. Supercrit. Fluids 135 (2018) 180–187, https://doi.org/10.1016/j.supflu.2018.01.024.
- [23] L. Mascia, G.Del Re, P.P. Ponti, S. Bologna, G.Di Giacomo, B. Haworth, Crystallization effects on autoclave foaming of polycarbonate using supercritical carbon dioxide, Adv. Polym. Technol. 25 (2006) 225–235, https://doi.org/ 10.1002/adv.20075.
- [24] M. Haurat, M. Dumon, Amorphous Polymers' foaming and blends with organic Foaming-Aid structured additives in supercritical CO2, a way to fabricate porous polymers from macro to nano porosities in batch or continuous processes, Molecules 25 (2020), https://doi.org/10.3390/MOLECULES25225320.
- [25] V. Bernardo, J. Martin-de Leon, I. Sanchez-Calderon, E. Laguna-Gutierrez, M. A. Rodriguez-Perez, Nanocellular polymers with a gradient cellular structure based on poly(methyl methacrylate)/thermoplastic polyurethane blends produced by gas dissolution foaming, Macromol. Mater. Eng. 305 (2020), https://doi.org/10.1002/mame.201900428.
- [26] E. Laguna-Gutierrez, J. Escudero, V. Kumar, M.A. Rodriguez-Perez, Microcellular foaming by using subcritical CO2 of crosslinked and non-crosslinked LDPE/clay nanocomposites, J. Cell. Plast. 54 (2018) 257–282, https://doi.org/10.1177/ 0021955X16681451.
- [27] B. Krause, R. Mettinkhof, N.F.A. Van Der Vegt, M. Wessling, Microcellular foaming of amorphous high-Tg polymers using carbon dioxide, Macromolecules 34 (2001) 874–884, https://doi.org/10.1021/ma001291z.
- [28] J. Martín-de León, V. Bernardo, M. ángel Rodríguez-Pérez, Low density nanocellular polymers based on PMMA produced by gas dissolution foaming: fabrication and cellular structure characterization, Polymers 8 (2016), https://doi. org/10.3390/polym8070265.
- [29] D. Tammaro, V. Contaldi, M.G.P. Carbone, E. Di Maio, S. Iannace, A novel lab-scale batch foaming equipment: the mini-batch, J. Cell. Plast. 52 (2016) 533–543, https://doi.org/10.1177/0021955X15584654.
- [30] M. Haurat, Y. Anguy, C. Gaborieau, G. Aubert, C. Aymonier, M. Dumon, Highpressure drop rates in solid-state batch one-step scCO2 foaming of acrylic polymers: a way to stabilize the structure of micro-nano foams, Chem. Eng. Sci. 281 (2023), https://doi.org/10.1016/j.ces.2023.119099.
- [31] Z. Xing, G. Wu, S. Huang, S. Chen, H. Zeng, Preparation of microcellular cross-linked polyethylene foams by a radiation and supercritical carbon dioxide approach, J. Supercrit. Fluids 47 (2008) 281–289, https://doi.org/10.1016/j.supflu.2008.08.009.
- [32] J. Pinto, M. Dumon, M. Pedros, J. Reglero, M.A. Rodriguez-Perez, Nanocellular CO2 foaming of PMMA assisted by block copolymer nanostructuration, Chem. Eng. J. 243 (2014) 428–435, https://doi.org/10.1016/j.cej.2014.01.021.
- [33] S. Wen, L. Yu, A.D. Phule, Y. Zhao, X. Zhang, Z.X. Zhang, Influence of 1-butene content on mechanical, thermal, and cushioning properties of propylene/1-butene copolymer foamed by supercritical carbon dioxide, J. Supercrit. Fluids 165 (2020), https://doi.org/10.1016/j.supflu.2020.104987.
- [34] J.A. Sarver, E. Kiran, Foaming of polymers with carbon dioxide the year-in-review 2019, J. Supercrit. Fluids 173 (2021) 105166, https://doi.org/10.1016/J. SUPFLU.2021.105166.
- [35] E. Di Maio, E. Kiran, Foaming of polymers with supercritical fluids and perspectives on the current knowledge gaps and challenges, J. Supercrit. Fluids 134 (2018) 157–166, https://doi.org/10.1016/J.SUPFLU.2017.11.013.
- [36] G. Brunner, Near critical and supercritical water. Part I. Hydrolytic and hydrothermal processes, J. Supercrit. Fluids 47 (2009) 373–381, https://doi.org/ 10.1016/j.supflu.2008.09.002.

- [37] R.M. Smith, Extractions with superheated water, 2002. (www.elsevier.com/locate/chroma)
- [38] D. Bröll, C. Kaul, A. Krämer, P. Krammer, T. Richter, M. Jung, H. Vogel, P. Zehner, Chemistry in supercritical water, Angew. Chem. Int. Ed. 38 (1999) 2998–3014, https://doi.org/10.1002/(SICI)1521-3773(19991018)38:20<2998::AID-ANIE2998>3.0.CO;2-L.
- [39] S.S. Toor, L. Rosendahl, A. Rudolf, Hydrothermal liquefaction of biomass: a review of subcritical water technologies, Energy 36 (2011) 2328–2342, https://doi.org/ 10.1016/j.energy.2011.03.013.
- [40] A. Fernández, A. Redondo, J. Martín-de-León, D. Cantero, PMMA stability under hydrothermal conditions, J. Supercrit. Fluids 198 (2023), https://doi.org/ 10.1016/j.supflu.2023.105938.
- [41] J. Pinto, E. Solórzano, M.A. Rodriguez-Perez, J.A. De Saja, Characterization of the cellular structure based on user-interactive image analysis procedures, J. Cell. Plast. 49 (2013) 555–575, https://doi.org/10.1177/0021955X13503847.
- [42] B. Notario, A. Ballesteros, J. Pinto, M.A. Rodríguez-Pérez, Nanoporous PMMA: a novel system with different acoustic properties, Mater. Lett. 168 (2016) 76–79, https://doi.org/10.1016/j.matlet.2016.01.037.
- [43] B. Notario, J. Pinto, M.A. Rodríguez-Pérez, Towards a new generation of polymeric foams: PMMA nanocellular foams with enhanced physical properties, Polymer 63 (2015) 116–126, https://doi.org/10.1016/j.polymer.2015.03.003.

- [44] J.M. de León, V. Bernardo, E. Laguna-Gutiérrez, M.Á. Rodríguez-Pérez, Influence of the viscosity of poly(methyl methacrylate) on the cellular structure of nanocellular materials, Polym. Int. 69 (2020) 72–83, https://doi.org/10.1002/pi.5920.
- [45] J. Pinto, S. Pardo, E. Solorzano, M.A. Rodriguez-Perez, M. Dumon, J.A. De Saja, Solid skin characterization of PMMA/MAM foams fabricated by gas dissolution foaming over a range of pressures, in: Defect and Diffusion Forum, Trans Tech Publications Ltd, 2012, pp. 434–439, https://doi.org/10.4028/www.scientific.net/ DDF.326-328.434.
- [46] V. Kumar, J.E. Weller, A model for the unfoamed skin on microcellular foams, Polym. Eng. Sci. 34 (1994).
- [47] Y. Fujii, T. Tominaga, D. Murakami, M. Tanaka, H. Seto, Local dynamics of the hydration water and Poly(Methyl Methacrylate) chains in PMMA networks, Front. Chem. 9 (2021), https://doi.org/10.3389/fchem.2021.728738.
- [48] Q. Guo, J. Wang, C.B. Park, M. Ohshima, A microcellular foaming simulation system with a high pressure-drop rate, Ind. Eng. Chem. Res. 45 (2006) 6153–6161, https://doi.org/10.1021/ie060105w.
- [49] S. Amherst, Preparation and characterization of microcellular foams processed in supercritical carbon dioxide, 1999. https://doi.org/10.7275/gg46-tm86.